Journal of Innovative Materials in Extreme Conditions
2026
Volume 7
Issue 1

# POLYMER-DERIVED CERAMIC ROUTE FOR THE SYNTHESIS OF ELECTRICALLY CONDUCTING $LaC_2/LaB_6$ CERAMIC NANOCOMPOSITES

***Hema Dinesh BARNANA[1], Gokul NANDA[1], Ganesh Babu THIYAGARAJAN[1], Nithin CHANDRAN B S[1], Renjith DEVASIA[2]*, and Ravi KUMAR[1,3]****

*[1]Laboratory of High-Performance Ceramics, Department of Metallurgical and Materials Engineering, Research Center on Ceramic Technologies for Futuristic Mobility, Indian Institute of Technology-Madras (IIT Madras), Chennai 600036, India.*

*[2]Ceramic Matrix Products Division, Analytical Spectroscopy and Ceramics Group, PCM Entity, Vikram Sarabhai Space Center (VSSC), ISRO, Thiruvananthapuram 695022, India.*

*[3]School of Sustainability, Indian Institute of Technology Madras (IIT Madras), Chennai 600036, India*

**Corresponding authors: d_renjith@vssc.gov.in and nvrk@iitm.ac.in*

**Abstract:** *Electrically conducting $LaC_2/LaB_6$ ceramic nanocomposites with a low coefficient of linear thermal expansion (CTE) were prepared through ceramization of single-source polymeric precursors containing La, B, and C. To synthesize such ceramics, phenol formaldehyde (PF) resin was reacted with precursors of La and B in various ratios to obtain single-source precursors of boron- and lanthanum-modified PF (hereafter referred to as B-Lamp). The precursors were characterized using thermogravimetry and spectrochemical techniques. The ceramic yield and phase crystallization, such as $LaC_2$ and $LaB_6$, were found to be profoundly influenced by the precursor ratio. The phase evolution and stability at various temperatures were investigated using X-ray diffraction, Raman spectroscopy, and high-resolution transmission electron microscopy, which reveals the presence of $B_4C$ as a competing phase in addition to the $LaC_2/LaB_6$ phases. The pyrolyzed ceramic powder was spark plasma sintered and evaluated for its electrical conductivity, which was ~0.56 S/cm, and CTE of $5 \times 10^{-6}$ /°C.*

**Keywords:** *Polymer-derived ceramics, coefficient of linear thermal expansion, lanthanum carbide, and lanthanum hexaboride*

## 1. Introduction

Electrically conducting ceramics find applications in various fields, including thermistors, gas sensors, electrodes, heating elements, thermoelectric generators, fuel cells, and batteries, and exemplify high potential due to their high chemical and thermal stability [1-3]. Also, they exhibit electrical conductivity > $10^{-2}$ S/cm, have high melting points (usually > 1500 °C), and have lower CTE (usually < 6 x $10^{-6}$/°C) than many electrically conductive metals. Rare-earth and transition-metal borides and carbides fall into this category and are being developed to replace tungsten- or molybdenum-based materials for electrical conductivity applications [4]. In which lanthanum dicarbide ($LaC_2$), a very high melting point phase is known to show metallic-like electrical conductivity which approaches that of lanthanum (18 S/cm) itself [5]. Using a single element (lanthanum) to form both the boride and the carbide prevents the formation of any intermediate compounds, such as rare-earth zirconates, which are typically observed when using multiple metals [6].

The synthesis of borides and carbides has been reported using various methods, including solid-state reactions, melt electrolysis, metal-gas reactions, combustion synthesis, and carbothermal reduction reactions. However, these techniques face challenges in achieving chemical homogeneity, purity, and a uniform microstructural composition [3]. These issues can be overcome by using the precursor-derived route to synthesize ceramics. The molecular structure of inorganic or organometallic precursors can be tailored to get compositions that would otherwise be impossible through conventional routes [7-8]. The ease of shaping the polymer to obtain near-net-shaped ceramic products for technological applications is also beneficial. In addition, the ceramics can be derived at relatively lower temperatures, making it advantageous over other routes described above.

Thus, this work aims to synthesize a lanthanum-based ceramic nanocomposite via a polymer-derived ceramic (PDC) route, study its phase evolution, and determine its suitability as an electrical conductor. To that end, lanthanum acetylacetonate hydrate and phenolic resin are chosen as initial precursors to synthesize a single-source precursor (SSP) of lanthanum and carbon. The stabilization of lanthanum carbide is facilitated by glassy carbon, which is formed from a phenolic resin [9-11], but this also increases the system's carbon content. The presence of free carbon has disadvantages, including poor oxidation resistance [12], and lower shear strength. Hence, to reduce the effective free carbon and its adverse effects on the system, boron is intentionally added to react with synthesized La and C SSPs, offering the following advantages. Boron is a well-known dopant used in glassy carbon, derived from phenolic resin, and carbon/carbon composites to enhance oxidation resistance [12-14]. Additionally, it was reported earlier that the addition of boron forms intermetallic solid solutions with metal matrix ceramic composites, which improve toughness through grain growth retardation, transformation toughening, crack impediment, and crack deflection or microcracking mechanisms [15-16]. Furthermore, it reduces the final oxygen in the ceramics [17]. Due to the lower formation temperature of boron carbide (<1500 °C), the addition of boron contributes to the formation of the boron carbide phase, which exhibits good thermoelectric properties, has a high melting point [18-19], and high oxidation resistance [20]. Moreover, as an added advantage, $LaB_6$ can be formed, which is known to exhibit excellent electrical conductivity owing to the spare electron available after the donation of two electrons to the boron sublattice [3,21]. Further, boron carbide acts as a catalyst or reducing agent by lowering the phase-evolution temperatures of borides and carbides relative to individual reducing agents such as carbon, boron, and aluminum [22-23].

In this work, a novel single-source precursor containing La, B, and C was synthesized for the first time via a polymer-derived ceramics route. The composition of the precursors was varied and correlated with the phase evolution upon ceramic conversion. The converted ceramic was also spark-plasma sintered to form a monolith and evaluated for its coefficient of linear thermal expansion and electrical conductivity.

## 2. Experimental methods

### 2.1. Materials

Materials used for synthesis of La-B-C precursor were phenol formaldehyde resin (PF) (as received from VSSC, Thiruvananthapuram, India, see Table 1), lanthanum acetylacetonate hydrate $La(CH_3COCHCOCH_3)_3$ x $H_2O$, denoted as $La(acac)_3$, (Sigma Aldrich, India), $B(OH)_3$ (99.5%, Sigma Aldrich, India), and N, N-dimethyl formaldehyde (DMF) (99.8% purity, Rankem, India) was used as a solvent.

**Table 1**. Specification of phenol formaldehyde resin

| Property | Phenolic resin |
|---|---|
| Type | Resol |
| Specific Gravity | 1.18-1.20 |
| Viscosity at 30 °C (cps) | 600 |
| Free formaldehyde (%) | 0.1 |
| Cure time | 120 min at 175 °C |

### 2.2 Synthesis of lanthanum-modified phenolic formaldehyde resin (Lamp)

PF and $La(acac)_3$ were dissolved in DMF and reacted at 120 °C for 4 h. The obtained lanthanum-modified phenol formaldehyde resin was named Lamp. Various Lamp compositions were prepared as

listed in Table 2. Beyond Lamp-30 (30 parts per hundred (pph) of $La(acac)_3$ w.r.t. PF), the resin starts precipitating out due to steric hindrance. Thus, Lamp-30 was selected as a suitable composition for further modification with $B(OH)_3$ to yield a boron-modified Lamp.

**Table 2**. No. of parts of $La(acac)_3$ used per 100 parts of PF to prepare different compositions of Lamp's

| S.No | No. of parts of PF (A) | No. of parts of $La(acac)_3$ (B) | No. of parts $La(acac)_3$ per hundred parts of PF | Lanthanum modified PF(Lamp) (A + B) (pph) |
|---|---|---|---|---|
| 1 | 100 | 10 | 10 | Lamp-10 |
| 2 | 100 | 20 | 20 | Lamp-20 |
| 3 | 100 | 30 | 30 | Lamp-30 |
| 4 | 100 | 40 | 40 | Lamp-40 |
| 5 | 100 | 50 | 50 | Lamp-50 |

### 2.3 Synthesis of boron-modified Lamp (B-Lamp)

Similar to the synthesis of Lamp, $B(OH)_3$ in DMF was reacted with Lamp-30 at 120 °C for 6 h. The resultant precursor, i.e., boron and lanthanum-modified PF was named as B-Lamp. Different compositions of B-Lamp were synthesized by gradually increasing the molar ratio of B to La, as shown in Table 3.

**Table 3**. Different molar ratios of $B(OH)_3$ added to the Lamp with respect to $La(acac)_3$ and PF to obtain various compositions of B-Lamp's

| S.No | Molar ratio (B:La) | Boron modified Lamp (B-Lamp) | Ceramized B-Lamp (BLaC) |
|---|---|---|---|
| 1 | 1:1 | 1B-Lamp | 1BLaC |
| 2 | 3:1 | 3B-Lamp | 3BLaC |
| 3 | 5:1 | 5B-Lamp | 5BLaC |
| 4 | 7:1 | 7B-Lamp | 7BLaC |
| 5 | 9:1 | 9B-Lamp | 9BLaC |
| 6 | 11:1 | 11B-Lamp | 11BLaC |
| 7 | 13:1 | 13B-Lamp | 13BLaC |

### 2.4 Ceramic conversion, sintering, and characterization methods

The synthesized Lamp and B-Lamp precursors were cross-linked at 250 °C in an oven for 4h. Fourier-transform infrared spectroscopy (FTIR) analysis (Jasco FT/IR-4100) of the crosslinked Lamp and B-Lamp polymers was carried out to understand the bonding characteristics of the modified phenolic resin. Thermogravimetric analysis (TA SDT Q600) of the crosslinked B-Lamp polymers was performed under constant argon flow at a heating rate of 10 °C/min from room temperature to 1000 °C to characterize thermal decomposition and ceramic yield.

The crosslinked polymers were pyrolyzed in a tubular furnace at 1600 °C for 3 h under argon to obtain BLaC ceramics. The ceramic powders of 9BLaC were selected, ground to fine powder in a mortar and pestle, and sintered using SPS (Dr Sinter SPS-500, Sumitomo Metals, Japan) at 1600 °C and 50 MPa pressure for 10 minutes under vacuum. Graphite foils were placed between the powder and die to prevent adherence between them. Phenolic resin pyrolyzed in identical conditions does not sinter and remains a powder during SPS in these conditions. However, it sinters to maximum density when it is modified with a boron precursor, which acts as a sintering aid. The ceramic powders and sintered pellets were subjected

to X-ray diffraction (Bruker AXS D8 Discover X-ray Diffractometer) at 30 kV using Cu $K_\alpha$ radiation (step scan of 0.075, count time 1 step/sec, and wavelength 0.154 nm) to determine the phases formed during heat treatment and sintering. The crystallite size (D) of $LaB_6$ in 9BLaC was measured using Scherrer's equation (Equation 1), assuming the shape of the particles to be spherical, and was found to be approximately 53 nm.

$$D = \frac{K\lambda}{\beta cos\theta} \quad (1)$$

Where *D* is the mean size of the ordered (crystalline) domains, which may be smaller or equal to the grain size; *K* is a dimensionless shape factor, taken as 0.9; $\lambda$ is the X-ray wavelength; $\beta$ is the line broadening at half the maximum intensity (FWHM) in radians; $\theta$ is the Bragg angle.

The presence of carbon and other ceramic phases was evaluated using Raman spectroscopy recorded with an alpha300R confocal Raman microscope with a Nd: YAG laser source with a wavelength of 532 nm. The ceramic powders are dispersed in ethanol using ultrasonication and drop cast onto a carbon-coated copper grid before being subjected to a high-resolution transmission electron microscope (HR-TEM JEOL 3010 with UHR polepiece, $LaB_6$ filament, and Scherrer's defocus of 0.12 nm). Scanning electron micrographs of the cross-section of the pellet were taken using Thermo Fisher Scientific Apreo S field emission scanning electron microscope (FESEM) and energy dispersive spectroscopy (EDS) (Accelerating voltage 0.5 to 30kV). Electrical I-V resistivity of the sintered pellet with respect to the change in temperature was measured using a ZEM 3 (ADVANCE RIKO, Inc.) from 30 °C to 200 °C under a vacuum atmosphere. The linear coefficient of thermal expansion was measured using a dilatometer (DIL 402 Expedis, Netzsch) from 130 °C to 1550 °C with a heating rate of 10 °C/min under an argon atmosphere.

## 3. Results

### 3.1 Spectrochemical characterization of crosslinked Lamp and B-Lamp polymers

Figure 1 (a) shows FT-IR spectra of Lamp resins and PF. In PF, the bands at 3430, 2925, 1610, 1480, 1390, 1153, and 1045 $cm^{-1}$ represent the O-H, $CH_2$ alkane, C=C aromatic, $CH_2$ methylene bridge, OH phenol, C-O stretch, and single stretch C-O vibrations of $CH_2OH$ methylene groups, respectively [24-26]. In Lamp, the band which appears around 3430, 2925, 1640, 1475, 1370, 1200, 1096, 1014, 652 $cm^{-1}$ are congruous with the O-H, $CH_2$ alkane, C=C, $CH_2$ aliphatic methylene, a phenol hydroxyl group, C-O, C-O-C, C-O vibrations of $CH_2$ methylene bridge, and La-O-C stretching, respectively [27-29]. Above Lamp-30, precipitation of individual precursors was observed. Thus, Lamp-30 is chosen for further modification with a boron precursor.

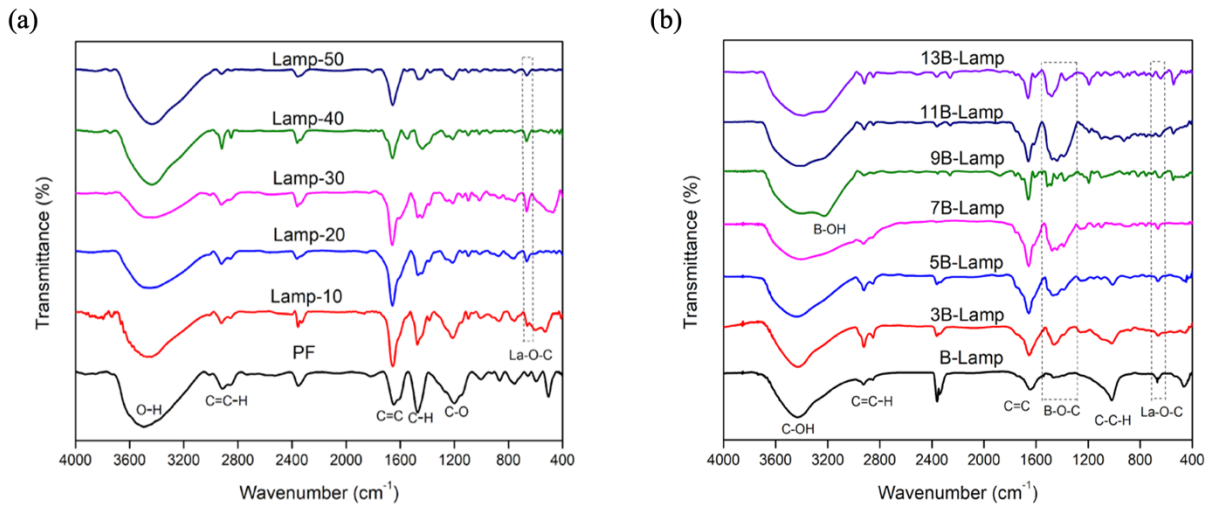


**Figure 1.** FT-IR spectra of (a)Lamp resins showing the formation of La-O-C bonds, (b)Lamp showing the formation of B-O-C bonds between methyl groups of acetylacetonates, unreacted hydroxyl groups of Lamp, and $B(OH)_3$.

Figure 1 (b) shows the FT-IR spectra of B-Lamps indicating the formation of B-O-C bands in the range of 1390 and 1480 $cm^{-1}$. The bands at 3446, 3220, 2916, 1640, 1483, 1390, 1000, and 652 $cm^{-1}$ match CO-H, BO-H, $CH_2$ alkane, C=C, C-H vibrations of aliphatic methylene, phenol C-OH, C-H, and La-O-C, respectively [30]. From B-Lamp to 11B-Lamp, as the boric acid content increases, the CO-H band intensity at 3460 $cm^{-1}$ decreases and broadens towards 3220 $cm^{-1}$, corresponding to the BO-H bands. Figure 2 (a) shows the TGA data of crosslinked B-Lamp polymers. With an increase in boron content from 1B-Lamp to 11B-Lamp, the ceramic yield also increases. However, the sudden drop in the ceramic yield of 13B-Lamp may be attributed to steric hindrance. The yield of 1B-Lamp is ≈ 53 % at 1000 °C, which increases to ≈ 62 % in 11B-Lamp.

### 3.3 Phase evolution studies of BLaC ceramics heat-treated at 1600 °C

Figure 2 (b) shows the XRDs of BLaC ceramic samples after pyrolysis at 1600 °C in an argon atmosphere for 3 h. The following peaks of 2θ values at 21.4, 30.4, 37.9, 43.5, 49.0, 54.0, 63.2, 67.6, and 71.8 ° corresponds to (100), (110), (111), (200), (210), (211), (220), (221), (310) planes of $LaB_6$ (ICDD reference pattern 01-075-1414) [31-33]. In 7BLaC and 9BLaC, the peaks appearing at 2θ 25.6, 26.4, and 44.5 ° are congruous with (100), (200) planes of $LaC_2$ (ICDD reference pattern 01-089-2255) [34-36]. The $LaB_6$ peaks first appear in 3BLaC, and the intensity of the peaks increases up to 9BLaC. 11BLaC exhibits peaks of $LaB_6$ with low intensity, but interestingly, it also showed the highest ceramic yield during thermogravimetric analysis.

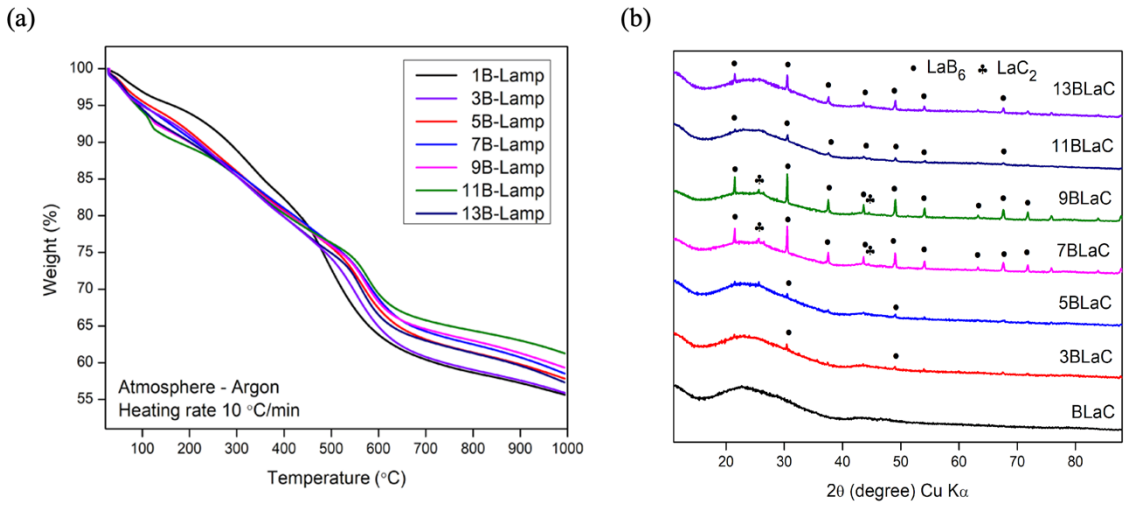


**Figure 2**. (a) TGA graph of B-Lamp preceramic polymers showing the increase in final ceramic yield at 1000 °C with the increase in boron precursor up to 11B-Lamp. (b) XRD of BLaC series ceramics revealing the formation of $LaB_6$ and $LaC_2$ phases in 9BLaC and 11BLaC compositions after pyrolysis at 1600 °C in an argon atmosphere for 3 h.

### 3.4 FT-IR analysis of BLaC ceramics

Figure 3 (a) shows the FT-IR of BLaC ceramics pyrolyzed at 1600 °C. The bands which appear around 3438, 2930, 1579, 1384, 1087 $cm^{-1}$ correspond to the stretching of $B_4C$ [37]. The band at 2930 $cm^{-1}$ is attributed to the C-H vibrations of the alkane on the aromatic ring [24]. The band at 1579 $cm^{-1}$ corresponds to the B-C vibrations of the inter-icosahedral C-B-C chains, and the strong peak at 1087 $cm^{-1}$ indicates the icosahedral structure of the $B_4C$ [38].

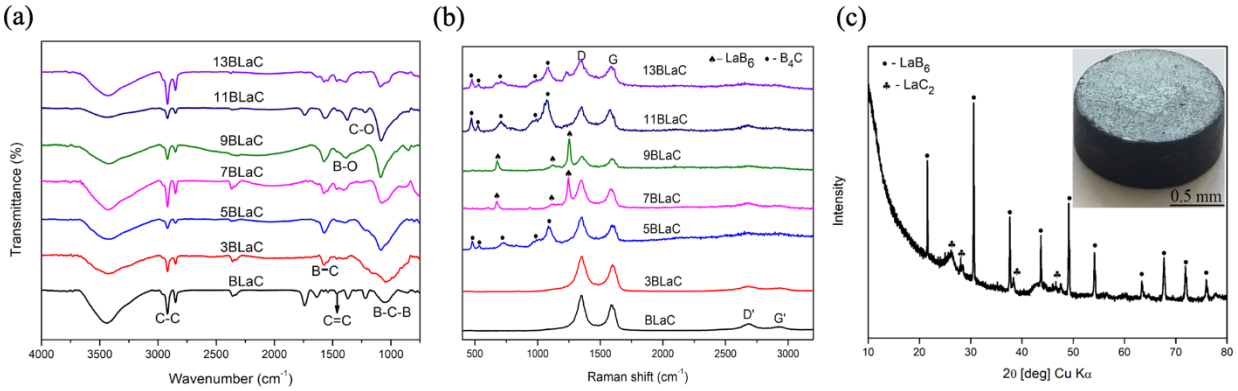


**Figure 3.** (a) FTIR spectrum of BLaC series ceramics heat-treated at 1600 °C showing the B-C-B bands at 1087 $cm^{-1}$. (b) Raman spectra of BLaC series ceramics showing bands of crystalline boron carbide at 481, 531, 730, 1000, 1086 $cm^{-1}$, $LaB_6$ bands at 672, 1128, 1247 $cm^{-1}$. (c) X-ray diffractogram of spark plasma sintered 9BLaC pellet showing crystalline phases of $LaC_2$ and $LaB_6$.

### 3.5 Raman spectra of BLaC ceramics

Figure 3 (b) shows the Raman spectra of the B-LaC ceramics after pyrolysis at 1600 °C. In the BLaC ceramics, two specific absorption peaks were observed at 1347 $cm^{-1}$ (D band) and 1589 $cm^{-1}$ (G

band), indicating the presence of free carbon in the system. In 7BLaC and 9BLaC, the bands at 672, 1128, 1247 $cm^{-1}$ are from $LaB_6$ Raman active vibrational modes of $T_{2g}$, $E_g$, and $A_{1g}$, respectively [39-40]. The bands at 481, 531, 730, 1000, and 1086 $cm^{-1}$ correspond to stretching vibrations of crystalline C-B-C chains, implying the presence of crystalline boron carbide in 5BLaC, 11BLaC, and 13BLaC [41-43]. After analyzing the TGA, XRD, FTIR, and Raman spectra of all the BlaC compositions, 9BlaC composition with the desired phases was chosen for sintering and further characterization.

### 3.6 XRD of sintered 9BLaC pellet

Figure 3 (c) shows the XRD data of spark plasma sintered 9BLaC, demonstrating the crystalline phases of $LaC_2$ and $LaB_6$. No new phase formation was observed after SPS to consolidate the powders.

### 3.7 Scanning electron microscopy

Figure 4 shows the cross-sectional SEM images of the sintered 9BLaC pellet. Figure 4 (a) shows the image in back-scattered mode, in which the brighter region indicates the lanthanum-rich phases like $LaB_6$ and $LaC_2$. Figure 4 (c) shows the images in secondary electron mode of the surface topography of the pellet. Figure 7 (b) EDAX showing the $K_\alpha$, $K_\beta$ of Lanthanum. Figure 4 (d) EDAX shows the distribution of lanthanum in a carbon matrix. There were no pores observed in the SEM images, indicating that the ceramic was sintered to maximum density. The density calculated using the water displacement method was 2.39 g/cc.

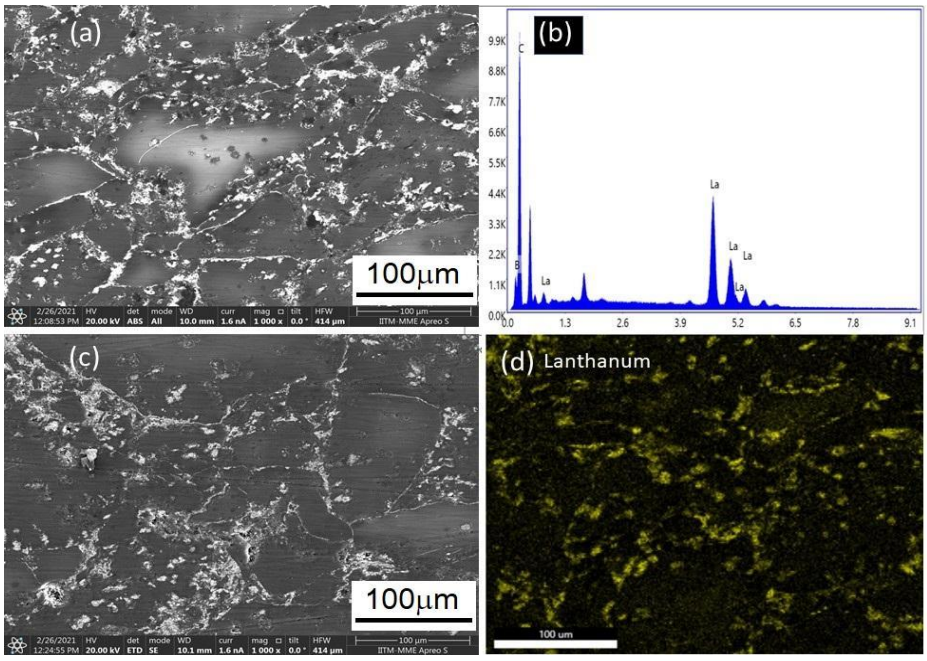


**Figure 4.** (a, c) SEM micrographs of 9BLaC ceramic nanocomposite under backscattered and secondary electron mode; (b, d) Elemental mapping of lanthanum and boron in a carbon matrix.

### 3.8 Microstructural characterization

Figure 5 shows HR-TEM micrographs of 9BLaC heat-treated at 1600 °C. In 9BLaC, the d spacing of 0.41 nm corresponds to $LaB_6$ [44]. The d spacing of 0.34 nm corresponds to $LaC_2$, representing the encapsulation of lanthanum in carbon [10]. The d spacing of 0.54 nm in 9BLaC is due to the fullerene structure of the carbon.

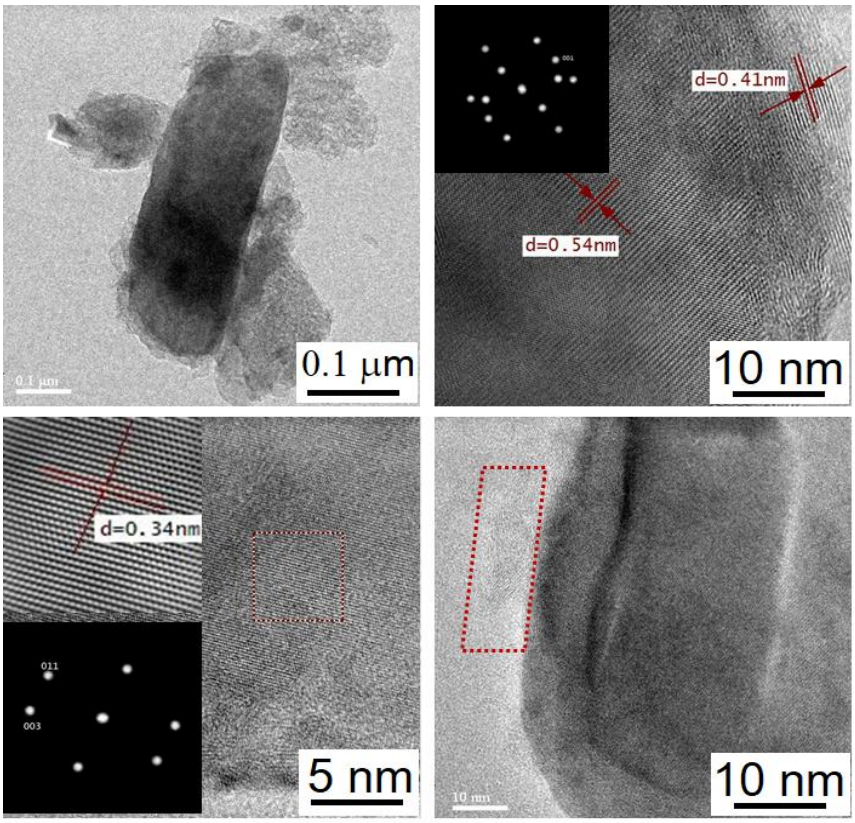


**Figure 5.** HR-TEM micrographs of 9BLaC ceramic nanocomposite reveal the existence of $LaB_6$, $LaC_2$, and free carbon (refined with Gatan GMS3 software).

### 3.9 Electrical properties

Figure 6 (a) shows the change in resistivity of the spark plasma sintered 9BLaC pellet with the variation in temperature from 25 °C to 200 °C. The values of resistivity do not change much as the temperature increases. The average resistivity offered by the pellet against the flow of electric current through it over the range of temperature was found to be 1.34 x $10^{-3}$ ohms cm. The electrical conductivity was found to be 7.46 x $10^{4}$ S/cm, which is very high when compared with similar ceramics such as zirconia (~ 1 x $10^{-4}$ S/cm) and silicon carbide (~ 1 x $10^{-2}$ S/cm) [45].

### 3.10 Thermal Properties

Figure 6 (b) shows the linear thermal expansion of sintered 9BLaC ceramic. The average coefficient of linear thermal expansion is found to be 4.9 x $10^{-6}$ /°C. The graph was divided into 4 regions with respect to the change in slope. The CTE of region 1, region 2, region 3, and region 4 are 4.26 x $10^{-6}$ /°C, 5.3 x $10^{-6}$ /°C, 5.6 x $10^{-6}$ /°C, and 4.1 x $10^{-6}$ /°C, respectively.

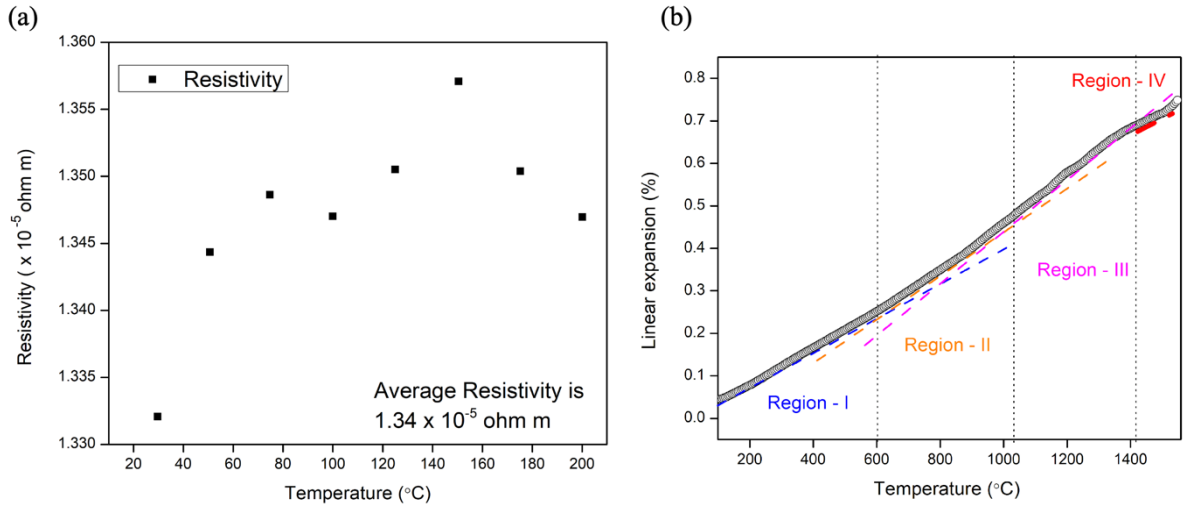


**Figure 6.** (a) Representing the change in the electrical resistivity with respect to the temperature for 9BLaC ceramic nanocomposite. (b) The 9BLaC ceramic nanocomposite exhibits a change in coefficient of linear thermal expansion as a function of temperature.

## 4. Discussion

### 4.1 Bonding characteristics of preceramic polymers Lamp & B-Lamp

In FT-IR analysis of the synthesized Lamp system (**section 2.2**), the appearance of La-O-C band at 652 $cm^{-1}$ and C-O stretching vibrations of C-O-C band at 1014 $cm^{-1}$ indicates the participation of more phenol and methylene hydroxyl groups in the reaction with $La(acac)_3$ [46]. During the synthesis of SSPs, with an increase in $La(acac)_3$ content above Lamp-10, reactivity initially increases due to the availability of more functional groups, then gradually decreases due to the reduction of active functional groups. There is also an increase in the bulkiness of $La(acac)_3$ functional groups around the phenolic resin due to steric hindrance, which prevents further reaction, leading to the precipitation of excess precursors during the synthesis. Thus, as shown in the results, Lamp-30 was selected and modified with boric acid to form B-Lamp precursors. In the FT-IR analysis of B-Lamp, the formation of B-O-C bands (**section 3.1**) is attributed to the reaction of $B(OH)_3$ with the methylene groups and leftover phenol hydroxyl of Lamp through a condensation reaction by elimination of water molecules [47-49].

### 4.2 Thermal degradation studies of B-Lamp

As shown in the TGA curve, thermal decomposition of unreacted acetylacetonate groups takes place above 250 °C [33]. From B-lamp to 11B-Lamp, the number of B-O-C bonds formed from the reaction with $La(acac)_3$ increases beyond 1B-Lamp, the number of unreacted acetylacetonate ligands will be less. This results in lesser degradation and higher ceramic yield with an increase in boron precursor at 1000 °C. However, in 13B-Lamp, many unreacted precursor molecules remain in the system as a result of the steric hindrance effect, which starts to evaporate during curing and heat-treatment, resulting in a lower ceramic yield.

### 4.3 Phase evolution studies

XRD analysis of the ceramics heat-treated at 1600 °C gives information on the phase evolution with respect to composition. With the increase in boron content from BLaC to 9BLaC, $LaB_6$ becomes the dominant phase. But in 11BLaC, the relative peak intensity of $LaB_6$ has decreased significantly. To understand this anomaly, FTIR and Raman spectra studies were done. FTIR and Raman spectra analysis of the ceramic powder samples confirm the presence of boron carbide, which was not seen in XRD. The Raman spectra results of BLaC ceramics reflect the phase evolution

observed in XRD. In 7BLaC and 9BLaC, where XRD shows intense peaks of $LaB_6$, Raman spectra correspondingly showed only crystalline $LaB_6$ bands. However, in 5BLaC and 11BLaC where the XRD exhibited $LaB_6$ peaks of low intensity, the Raman spectra show only the bands of boron carbide. Several authors have reported that high impact stresses can cause the amorphization of $B_4C$ by the interaction between B-C-B chain atoms and neighboring icosahedral C-B-C atoms, resulting in the distortion of the icosahedral structure [51-52].

Therefore, it can be supposed that the crystallization of $LaB_6$, causes stresses that distort the crystalline icosahedron of boron carbide, leading to amorphization. The absence of amorphous boron carbide Raman bands (1330 and 1810 $cm^{-1}$) in 7BLaC and 9BLaC confirms that the boron carbide does not just remain amorphous, but instead, is consumed towards the crystallization of $LaB_6$ and $LaC_2$. The inverse relationship between the amount of $LaB_6$ and boron carbide in XRD and Raman spectra implies a reaction where amorphous boron carbide is consumed to facilitate the growth of $LaB_6$ crystals. The consumption of $B_4C$ also seems to enable the formation of $LaC_2$, which is not seen at that same temperature in the corresponding ceramics in the absence of boron (LaC) as shown in Figure 7. Also, the compositions below 7BLaC will never undergo structural dissociation because there is not enough stoichiometric composition of boron present in the system, which is required for the crystallization of $LaB_6$.

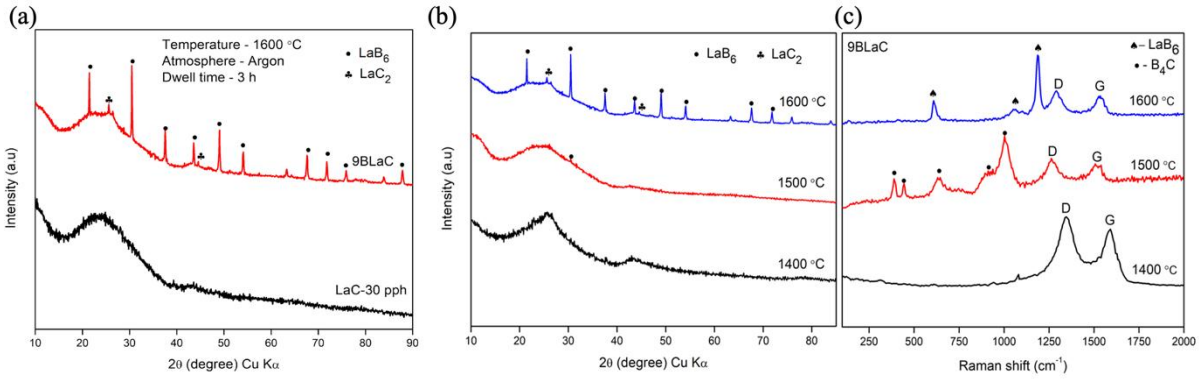


**Figure 7.** (a) XRD of LaC-30 pph & 9BLaC showing crystallization of $LaC_2$ only after incorporation of boron (9BLaC) on heat-treatment of ceramics at the same temperature (1600 °C). (b) X-ray diffractograms of 9BLaC heat-treated at different temperatures showing crystallization of $LaB_6$. (c) Raman spectra of 9BLaC revealing the phase evolution of boron carbide on heat-treating at different temperatures.

To explain this phenomenon further, 9BLaC was selected and heat-treated at 1400 °C, 1500 °C, and 1600 °C. Figure 12 (a) & (b) shows the XRD and Raman spectra, respectively, for the corresponding heat-treatments. For the ceramic heat-treated at 1400 °C, XRD is amorphous, and Raman spectra only show D and G bands of carbon. On annealing at 1500 °C, Raman spectra exhibit boron carbide bands, while XRD of the ceramic remains amorphous as expected. On further annealing at 1600 °C, XRD and Raman spectra confirm the presence of crystalline $LaB_6$. $LaC_2$ is also present but can only be seen in XRD since $LaC_2$ is not Raman active. Thus, we have experimental evidence on the amorphization of $B_4C$ and the subsequent consumption enabling crystallization of $LaB_6$ and $LaC_2$.

### 4.4 Electronic conduction mechanism of La-B-C ceramic nanocomposite

The electrical conductivity of pure phenolic resin when converted into ceramic nanocomposites by heat treating at 1000 °C is 2.5 x $10^2$ S/cm [53]. In electrical conductivity measurements of newly synthesized 9BLaC nanocomposites have shown two orders of higher electrical conductivity (7.46 x $10^4$ S/cm) when compared to carbon composite [34]. Since the $LaB_6$ is the major phase distributed in the fullerene carbon matrix of the 9BLaC ceramic nanocomposite, the

electrical conductivity of it is approaching that of pure $LaB_6$, i.e., 6.65 x $10^4$ S/cm, and thus $LaB_6$ likely to be responsible for the high conductivity of the La-B-C ceramic nanocomposite system.

### 4.5 Effect of $LaC_2$ on CTE of La-B-C ceramic nanocomposites

The major phases present in the 9BLaC system are $LaB_6$, $LaC_2$, and glassy carbon. Both $LaB_6$ and glassy carbon retain their phase structure till melting point. However, $LaC_2$ undergoes phase transformations with respect to temperature. Below 600 °C, the phase is known as $\alpha LaC_2$, and its crystal structure is tetragonal. It transforms into $\beta LaC_2$ above 1081 °C, which has a cubic structure [54] (**Section 3.11**). Change in compositional homogeneity of $LaC_2$ was responsible for little change in CTE from 600 °C to 1081 °C.

$$La + \beta LaC_2 \longrightarrow La_2C_3 \qquad (2)$$

$LaC_2$ undergoes a peritectic reaction by reaction with lanthanum above 1415 °C and transforms to $La_2C_3$ as shown in Equation (2) [55]. Thus, in all four regions, CTE change is mainly controlled by the change in composition and phase transformation of $LaC_2$ in 9BLaC ceramic nanocomposite.

## 5. Conclusions

In this work, ceramic nanocomposites of La-B-C were developed through a novel route derived from single-source precursors. The composition of the ceramic could be finely controlled by varying the ratio of $La(acac)_3$ and $B(OH)_3$ with respect to each other and phenolic resin. The reactions and the maximum amount of precursor that could react with phenolic resin were determined with the help of FTIR of the SSPs. An increase in thermal stability and ceramic yield was observed with the increase in $B(OH)_3$ content in the SSPs. Phase evolution studies, conducted through XRD and Raman spectroscopy, confirmed the crystallization of $LaB_6$ and $LaC_2$ phases in certain BLaC compositions, as well as boron carbide in other compositions. The ceramic composition 9BLaC was chosen for sintering and measurement of transport phenomenon due to a high ceramic yield and crystallization of desired $LaC_2$ and $LaB_6$ phases. The measured electrical conductivity was 7.46 x $10^4$ S/cm, which is very high when compared with other ceramics such as silicon carbide, zirconia, and alumina. 9BLaC showed a relatively low CTE of 4.96 x $10^{-6}$ /°C from room temperature to 1550 °C. The study demonstrated a novel pathway for synthesizing a thermally stable and electrically conducting ceramic for functional applications.

**References**


[1] Van de Goor G, Sägesser P, Berroth K (1997) Electrically conductive ceramic composites. *Solid State Ionics* 101–103:1163–1170.

[2] Mori T (2019) Thermoelectric and magnetic properties of rare earth borides : Boron cluster and layered compounds. *Journal of Solid State Chemistry* 275:70–82.

[3] Cahill JT, Graeve OA (2019) Hexaborides: A review of structure, synthesis and processing. J *Mater Res Technol* 8:6321–6335.

[4] Schönfeld K, Martin HP, Michaelis A (2017) Pressureless sintering of ZrC with variable stoichiometry. *J Adv Ceram* 6:165–175.

[5] Greenwood NN, Osborn AJ (1961) 345. Chemical and magnetic properties of lanthanum dicarbide and sesquicarbide. *J Chem Soc* 1775–1782.

[6] Nanda G, Thiyagarajan GB, Kumar KH, et al (2021) Novel class of precursor-derived Zr–La–B–C(O) based ceramics containing nano-crystalline ultra-high temperature phases stable beyond 1600 °C. *Ceram Int* 48:1981–1989.

[7] Ionescu E, Bernard S, Lucas R, et al (2019) Polymer-Derived Ultra-High Temperature Ceramics (UHTCs) and Related Materials. *Adv Eng Mater* 1900269:1–24.

[8] Namura M, Waki I, Sato Y, et al (2009) Preparation and characterization of lanthanum carbide encapsulated carbon nanocapsule/lanthanum hexaboride nanocomposites. *Mater Lett* 63:1307–1310.

[9] Colombo P, Mera G, Riedel R, Sorarù GD (2010) Polymer-derived ceramics: 40 Years of research and innovation in advanced ceramics. *J Am Ceram Soc* 93:1805–1837.

[10] Ionescu E, Bernard S, Lucas R, et al (2019) Polymer-Derived Ultra-High Temperature Ceramics (UHTCs) and Related Materials. *Adv Eng Mater* 1900269:1–24.

[11] Valencia R, Rodríguez-Fortea A, Poblet JM (2008) Understanding the stabilization of metal carbide endohedral fullerenes M2C2@C82 and related systems. *J Phys Chem A* 112:4550–4555.

[12] Liu M, Cowley JM (1995) Encapsulation of lanthanum carbide in carbon nanotubes and carbon nanoparticles. *Carbon N Y* 33:225–232.

[13] Namura M, Waki I, Sato Y, et al (2009) Preparation and characterization of lanthanum carbide encapsulated carbon nanocapsule/lanthanum hexaboride nanocomposites. *Mater Lett* 63:1307–1310.

[14] Sheehan JE (1989) Oxidation protection for carbon fiber composites. *Carbon N Y* 27:709–715.

[15] Kaur S, Mera G, Riedel R, Ionescu E (2016) Effect of boron incorporation on the phase composition and high-temperature behavior of polymer-derived silicon carbide. *J Eur Ceram Soc* 36:967–977.

[16] Namura M, Waki I (1997) Boron and Phosphorus Doped Glassy Carbon: Boron 35:1567–1572

[17] Telle R, Petzow G (1988) Strengthening and toughening of boride and carbide hard material composites. *Mater Sci Eng* 105–106:97–104.

[18] Zhang GJ, Ando M, Yang JF, et al (2004) Boron carbide and nitride as reactants for in situ synthesis of boride-containing ceramic composites. *J Eur Ceram Soc* 24:171–178.

[19] Goldstein A, Geffen Y, Goldenberg A (2001) Boron Carbide-Zirconium Boride in Situ Composites by the Reactive Pressureless Sintering of Boron Carbide-Zirconia Mixtures. J Am Ceram Soc 84:642–644.

[20] Gunnewiek RFK, Souto PM, Kiminami RHGA (2017) Synthesis of Nanocrystalline Boron Carbide by Direct Microwave Carbothermal Reduction of Boric Acid. *J Nanomater* 3, 20-11.

[21] Mondal S, Bykova E, Dey S, et al (2016) Disorder and defects are not intrinsic to boron carbide. *Sci Rep* 6:11–16.

[22] Li J, Luo R, Lin C, et al (2007) Oxidation resistance of a gradient self-healing coating for carbon/carbon composites. Carbon N Y 45:2471–2478.

[23] Mercurio J ~P., Etourneau J, Naslain R, Hagenmuller P (1976) Electrical and magnetic properties of some rare-earth hexaborides. *J Less Common Met* 47:175–180.

[24] Fahrenholtz WG, Hilmas GE, Talmy IG, Zaykoski JA (2007) Refractory diborides of

zirconium and hafnium. *J Am Ceram Soc* 90:1347–1364.
[25] Sonber JK, Murthy TSRC, Subramanian C, et al (2010) Investigations on synthesis of HfB2 and development of a new composite with TiSi2. *Int J Refract Met Hard Mater* 28:201–210.
[26] Poljanšek I, Krajnc M (2005) Characterization of phenol-formaldehyde prepolymer resins by in line FT-IR spectroscopy. *Acta Chim Slov* 52:238–244.
[27] Cardona F, Moscou C (2008) Synthesis and characterization of modified phenolic resins for composites with enhanced mechanical properties. *Futur Mech Struct Mater - Proc 20th Australas Conf Mech Struct Mater* ACMSM20 317–322.
[28] Lin C Te, Lee HT, Chen JK (2015) Preparation and properties of bisphenol-F based boron-phenolic resin/modified silicon nitride composites and their usage as binders for grinding wheels. Appl Surf Sci 330:1–9.
[29] Kumar PR, Maharajan TM, Prabu AP, et al (2019) Hydroxyl radical scavenging activity of La 2 O 3 nanoparticles. *Pharma Innov J* 8:759–763.
[30] Hussein GAM, Ismail HM (1995) Characterization of lanthanum oxide formed as a final decomposition product of lanthanum acetylacetonate: thermoanalytical, spectroscopic and microscopic studies. *Powder Technol* 84:185–190.
[31] I.N Ismaila, Z.A.M. Ishakb, M.F. Jaafara, S.Omara MFZA and, Marzukia H. A (2009) Thermomechanical Properties of toughened phenolic resol resin. *Solid State Sci Technol* 17:351–368
[32] Romanos J, Beckner M, Stalla D, et al (2013) Infrared study of boron-carbon chemical bonds in boron-doped activated carbon. Carbon N Y 54:208–214.
[33] Zhou S, Zhang J, Liu D, et al (2010) Synthesis and properties of nanostructured dense LaB6 cathodes by arc plasma and reactive spark plasma sintering. *Acta Mater* 58:4978–4985.
[34] Hasan MM, Sugo H, Kisi EH (2014) Low temperature synthesis of rare-earth hexaborides for solar energy conversion. *MATEC Web Conf* 13:0–4.
[35] John SK, Anappara AA (2020) Facile synthesis of aqueous-dispersed luminescent nanosheets from non-layered lanthanum hexaboride. *RSC Adv* 10:31788–31793.
[36] Carturan S, Tonezzer M, Piga L, et al (2007) Synthesis and characterization of lanthanum dicarbide-carbon targets for radioactive ion beams generation via the carbothermal reaction. *Nucl Instruments Methods Phys Res Sect A Accel Spectrometers, Detect Assoc Equip* 583:256–263.
[37] Dong L, Wang J, Liu W, et al (2015) Fabrication and thermionic emission properties of lanthanum carbide doped tungsten cathodes. *Mater Lett* 146:47–50.
[38] Qiting LI, Jiansen NI, Yiqing WU, et al (2011) Synthesis and characterization of La ( OH ) 3 nanopowders from hydrolysis of lanthanum carbide. *J Rare Earths* 29:416–419.
[39] Li X, Jiang D, Zhang J, et al (2013) The dispersion of boron carbide powder in aqueous media. *J Eur Ceram Soc* 33:1655–1663.
[40] Ahmed YMZ, El-Sheikh SM, Ewais EMM, et al (2017) Controlling the Morphology and Oxidation Resistance of Boron Carbide Synthesized Via Carbothermic Reduction Reaction. J Mater Eng Perform 26:1444–1454.
[41] Mattox TM, Chockkalingam S, Roh I, Urban JJ (2016) Evolution of Vibrational Properties in Lanthanum Hexaboride Nanocrystals.
[42] Selvan RK, Genish I, Perelshtein I, et al (2008) Single step, low-temperature synthesis of submicron-sized rare earth hexaborides. *J Phys Chem C* 112:1795–1802.
[43] Chauhan A, Schaefer MC, Haber RA, Hemker KJ (2019) Experimental observations of amorphization in stoichiometric and boron-rich boron carbide. Acta Mater 181:207–215.
[44] Yan XQ, Li WJ, Goto T, Chen MW (2006) Raman spectroscopy of pressure-induced amorphous
boron carbide. *Appl Phys Lett* 7, 88.
[45] Mishra A, Sahoo RK, Singh SK, Mishra BK (2015) Synthesis of low carbon boron carbide powder
using a minimal time processing route: *Thermal plasma. J Asian Ceram Soc* 3:373–376.
[46] Xu J, Hou G, Li H, et al (2013) Fabrication of vertically aligned single-crystalline lanthanum hexaboride nanowire arrays and investigation of their field emission. *NPG Asia Mater* 5:e53-9.

[47] Scholz R, Dos Santos Marques F, Riccardi B (2002) Electrical conductivity of silicon carbide composites and fibers. J Nucl Mater 307–311:1098–1101.
[48] Feng J, Chen L, Gu J, et al (2016) Synthesis and characterization of aryl boron-containing thermoplastic phenolic resin with high thermal decomposition temperature and char yield.
[49] ZMIHORSKA-GOTFRYD A (2006) Phenol-formaldehyde resols modified by boric acid. Polimery/Polymers 51:386–388.
[50] Ganesh Babu T, Devasia R (2016) Boron-modified phenol formaldehyde resin-based self-healing matrix for Cf/SiBOC composites. *Adv Appl Ceram* 115:457–469.
[51] Wu W, Leng J, Wang Z, et al (2016) Preparation, curing, and properties of boron-containing bisphenol-S formaldehyde resin/o-cresol formaldehyde epoxy resin/nano-SiO2 composites. *Macromol Res* 24:209–217.
[52] Hussein GAM, Ismail HM (1995) Characterization of lanthanum oxide formed as a final decomposition product of lanthanum acetylacetonate: thermoanalytical, spectroscopic and microscopic studies. *Powder Technol* 84:185–190.
[53] Chen M, McCauley JW, Hemker KJ (2003) Shock-induced localized amorphization in boron carbide. *Science* 299:1563–1566.
[54] Ge D, Domnich V, Juliano T, et al (2004) Structural damage in boron carbide under contact loading. *Acta Mater* 52:3921–3927.
[55] De Souza WO, Garcia K, De Avila Von Dollinger CF, Pardini LC (2015) Electrical behavior of carbon fiber/phenolic composite during pyrolysis. *Mater Res* 18:1209–1216.
[56] Polyakov O (2013) Chapter 18 - Technology of Ferroalloys with Rare-Earth Metals. In: Gasik M (ed) Handbook of Ferroalloys. Butterworth-Heinemann, Oxford, pp 459–469
[57] Babizhetskyy V, Kotur B, Levytskyy V, Michor H (2017) Chapter 298 - Alloy Systems and Compounds Containing Rare Earth Metals and Carbon. In: Bünzli J-CG, Pecharsky VK (eds) Including Actinides. Elsevier, pp 1–263